Dissipation in passive non-reciprocal Hall-effect microwave devices

Bosco, Stefano

DOI
10.1088/2633-4356/ae20ea

Publication date
2025

Document Version
Final published version

Published in
Materials for Quantum Technology

PAPER • **OPEN ACCESS**

Dissipation in passive non-reciprocal Hall-effect microwave devices

To cite this article: Stefano Bosco 2025 *Mater. Quantum. Technol.* **5** 046202

Materials for Quantum Technology

PAPER

OPEN ACCESS

RECEIVED
31 August 2025

REVISED
10 November 2025

ACCEPTED FOR PUBLICATION
18 November 2025

PUBLISHED
26 November 2025

Dissipation in passive non-reciprocal Hall-effect microwave devices

Stefano Bosco

QuTech and Kavli Institute of Nanoscience, Delft University of Technology, Lorentzweg 1, 2628 CJ Delft, The Netherlands

E-mail: s.bosco@tudelft.nl

Keywords: non-reciprocal devices, topological materials, anomalous Hall effect, quantum Hall effect, circulators, gyrators, dissipation

Abstract

Non-reciprocal devices are key components in both classical and quantum electronics. One approach to realizing passive non-reciprocal microwave devices is through capacitive coupling between external electrodes and materials exhibiting non-reciprocal conductance. In this work, we develop an analytic framework that captures the response of such devices in the presence of dissipation while accounting for the full AC dynamics of the material. Our results yield an effective circuit model that accurately describes the device response in experimentally relevant regimes even at small dissipation levels. Furthermore, our analysis reveals counterpropagating features arising from the intrinsic AC response of the material that could be exploited to dynamically switch the non-reciprocity of the device, opening pathways for tunable non-reciprocal microwave technologies.

1. Introduction

Non-reciprocal devices are widely used to efficiently route signals and are essential in electronics, microwave photonics, and emerging quantum technologies [1]. Non-reciprocal effects have been proposed and realized in diverse platforms, including magnonics [2, 3], optomechanics [4–6], and heat transport [7]. More recently, superconducting non-reciprocal devices, for example based on the superconducting diode effect [8–15] or multi-terminal devices [16–20], have been suggested as a means to reduce power consumption in classical information processing [21, 22], as well as to provide new building blocks for quantum information systems [23–27]. Coherent non-reciprocal devices are being considered as candidates for encoding logical qubits when coupled to superconducting qubits [23] and can offer ways to entangle semiconducting qubits over long distances [28–32]

In current quantum technologies, low-loss microwave circulators are indispensable for directing the flow of quantum information and suppressing thermal noise [33]. State-of-the-art devices are typically passive components that exploit interference effects in combination with magnetic materials [34]. However, achieving microwave operation in the GHz regime restricts these devices to centimeter-scale footprints, which poses challenges for scalability and integration. Active non-reciprocal devices based on reservoir engineering [35] and metamaterials [36] have also been explored, but they require continuous external pumping, increasing complexity and heat. Combining phase delay and switches is also been actively studied as a way to enable circulation [37–39].

To overcome these limitations, compact passive devices have been proposed that rely on low-loss two-dimensional materials with intrinsic non-reciprocal conductance capacitively coupled to external leads [40]. Notable examples include topological materials in the quantum Hall regime [41–44], where non-reciprocal transport emerges under a strong perpendicular magnetic field, as well as anomalous quantum Hall systems that realize similar effects without large external fields [45–48]. These emerging material platforms open pathways to scalable, low-loss, and tunable non-reciprocal microwave technologies.

In this work, we present a general analytical description of this type of passive non-reciprocal devices that, in contrast to existing approaches [40, 49, 50], fully incorporates the effects of dissipation. We

consider the generic architecture sketched in figure 1(a), comprising a material with non-reciprocal conductance capacitively coupled to external driving electrodes. Our model is based on a semiclassical treatment of a Hall material subject to a magnetic field, where both non-reciprocity and losses are captured through the Hall angle θ_{H} [51]. This parameter interpolates between the reciprocal and dissipative regime ($\theta_{\mathrm{H}} = 0$) and the quantum Hall regime ($\theta_{\mathrm{H}} = \pi/2$), where transport is fully non-reciprocal and lossless.

Our model directly describes the response of devices implemented in several materials including e.g. gallium arsenide (GaAs) [40] and germanium [52], and allows us to describe a practically relevant regime of sub-Tesla magnetic fields where the quantized Hall plateaus are not fully developed and residual resistivity is finite. Moreover, our results also can be generalized to materials in the anomalous Hall phase [45] and graphene [53], that display low diagonal resistivity at low magnetic field [54] and room temperature [55], respectively.

Building on this framework, we derive an effective circuit model, shown in figure 1(b), which accurately captures the device response in the experimentally relevant limits of low losses and low frequencies. Our model can be generalized to incorporate the effect of the intrinsic AC response of the material, as well as additional sources of dielectric losses. For example, by including a finite kinetic inductance, our model reveals the presence of counterpropagating resonances. These features provide opportunities to selectively control the propagation direction of signals, offering a new route to dynamically tunable non-reciprocal microwave devices.

2. Microscopic model

We consider a semiclassical model of the device in figure 1(a), where the response of a two-dimensional system in the plane $\mathbf{r} = (x, y)$ is governed in the frequency domain by the coupled equations for the excess charge density ρ, scalar potential V, and current density $\mathbf{j}$ [56, 57]:

$$V(\mathbf{r}) = \bar{V}(\mathbf{r}) + \int \mathrm{d}\mathbf{r}' G(\mathbf{r}, \mathbf{r}')\, \rho(\mathbf{r}') \ , \tag{1a}$$

$$\mathrm{i}\omega \rho(\mathbf{r}) = \nabla \cdot \mathbf{j}(\mathbf{r}) \ , \tag{1b}$$

$$\mathbf{j}(\mathbf{r}) = -\underline{\sigma}(\mathbf{r}) \cdot \nabla V(\mathbf{r}) \ . \tag{1c}$$

Here, equation (1*a*) represents the inverted three-dimensional Poisson equation with the electrostatic Green's function G evaluated at the position of the two-dimensional electron gas, including the effect of an external drive $\bar{V}$. Equation (1*b*) is the continuity equation, while equation (1*c*) expresses Ohm's law, relating current density to the electric field through the local conductivity tensor.

When a perpendicular magnetic field B is applied, the Hall effect is captured by an antisymmetric local conductivity tensor. For concreteness, we restrict to a circular device of radius R characterized by

$$\underline{\sigma}(\mathbf{r}) = \sigma_0 n(r) \begin{pmatrix} \cos(\theta_{\mathrm{H}}) & \sin(\theta_{\mathrm{H}}) \\ -\sin(\theta_{\mathrm{H}}) & \cos(\theta_{\mathrm{H}}) \end{pmatrix} \ , \tag{2}$$

and work in cylindrical coordinates $\mathbf{r} = (r, \varphi)$. To account for spatial inhomogeneity, we introduce a dimensionless function $n(r)$, with support on $r \in [0, R]$, that interpolates from $n(0) = 1$ in the bulk of the material to $n(R) = 0$ at the edge over a characteristic length scale l.

Our results are applicable to the wide class of materials described by equation (2), which includes the family of quantum Hall [58] and anomalous Hall materials [59]. To more concretely and quantitatively estimate the AC response and losses in these devices, we consider the AC Drude model for a GaAs-etched droplet analogous to [41, 44]. This yields the conductivity scale and Hall angle

$$\sigma_0 = \frac{e^2 n_S \tau}{m^*} \frac{1}{\sqrt{(1 - \mathrm{i}\omega\tau)^2 + \omega_c^2 \tau^2}} \ , \tag{3a}$$

$$\theta_{\mathrm{H}} = \mathrm{arctan2}(\omega_c \tau, 1 - \mathrm{i}\omega\tau) \ , \tag{3b}$$

where n_S is the bulk electron density, τ a characteristic scattering time, m^* the effective mass, and $\omega_c = eB/m^*$ the cyclotron frequency. Explicitly for high-mobility GaAs [41] with effective mass $m^* = 0.067 m_0$, at magnetic field $B = 1\,\mathrm{T}$, density $n_S = 10^{11}\,\mathrm{cm}^{-2}$, and mobility $\mu = e\tau/m^* = 5 \times 10^6\,\mathrm{cm}^2/\mathrm{Vs}$, we find the cyclotron frequency $\omega_c/2\pi \approx 420\,\mathrm{GHz}$ and the scattering time $\tau \approx 0.19\,\mathrm{ns}$. At low frequency $\omega/2\pi \ll 33\,\mathrm{GHz}$ and low magnetic field, the conductivity prefactor is real-valued, i.e. $\sigma_0 \approx \sigma_0(\omega = \omega_c = 0) = e^2 n_S \tau/m^* \approx 1/12.5\ \Omega^{-1}$.

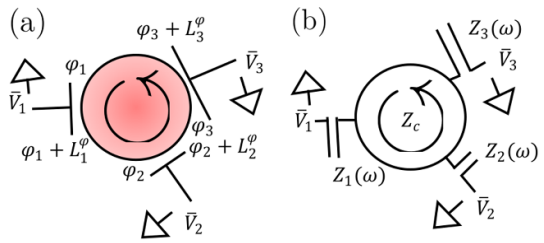

Figure 1. Device and circuit model. (a) Sketch of a device comprising a non-reciprocal material capacitively coupled to external electrode of angular length L_i^φ with potential $\bar{V}_i$ applied to a common ground. (b) The response of this device can be interpreted via a simple circuit model comprising an ideal circulator with characteristic impedance Z_c coupled to lossy stubs, i.e. transmission lines terminated in open circuits, with frequency dependent impedance $Z_i(\omega)$.

Combining equations (1*b*) and (1*c*), we obtain a differential equation relating ρ and V:

$$-\mathrm{i}\omega\rho = \sigma_0\left[n'\left(\sin\theta_\mathrm{H}\tfrac{\partial_\varphi}{r} + \cos\theta_\mathrm{H}\partial_r\right) + n\cos\theta_\mathrm{H}\nabla^2\right]V\,. \tag{4}$$

This equation reveals that without additional bulk charges, V satisfies the two-dimensional Laplace equation in the bulk of the material and the chiral dynamics of the excess charge along the perimeter is restricted to a small region close to the boundary where $n' = \partial_r n \neq 0$.

Substituting equation (4) into equation (1*a*) yields an integro-differential equation for the potential V [51]. This equation admits exact solutions in certain limits. In particular, for an infinitely sharp boundary and without external driving, Volkov and Mikhailov showed that a chirally propagating edge charge density (often referred to as edge magneto-plasmons) is redistributed into the bulk by long-range Coulomb interactions, over a length scale set by the kinetic inductance $\mathrm{Im}[\sigma_0\cos\theta_\mathrm{H}]$ [60]. For smoother edges, multiple edge-charge modes can emerge, each propagating with a distinct velocity [61].

3. General solution

3.1. Driven potential

The problem simplifies considerably under the local capacitance approximation [62], where the three-dimensional Poisson equation is replaced by the local relation

$$V \approx \bar{V} + \frac{\rho}{c}\,, \tag{5}$$

with capacitance per unit length c. If we also restrict ourselves to sharp interfaces with $l \to 0$, we find that $\rho \propto n' \approx -\delta(r-R)$ and the bulk potential satisfies the Laplace equation

$$\nabla^2 V = 0\,, \tag{6}$$

complemented by the capacitive boundary condition at $r = R$ [40]

$$\mathrm{i}\omega\left(V - \bar{V}(\varphi)\right) = \omega_R\left(\sin\theta_\mathrm{H}\partial_\varphi + R\cos\theta_\mathrm{H}\partial_r\right)V\,, \tag{7}$$

where we introduce the characteristic frequency

$$\omega_R = \frac{\sigma_0}{cR}\,. \tag{8}$$

The driving potential $\bar{V}$ is a function of the angle φ along the edge and in general it can be decomposed into Fourier harmonics as

$$\bar{V}(\varphi) = \sum_m \bar{v}_m \mathrm{e}^{\mathrm{i}m\varphi}\,. \tag{9}$$

Equation (7) shows that at $\theta_\mathrm{H} = \pi/2$, the boundary potential becomes decoupled from the bulk potential, and the device response is entirely governed by boundary plasmons that propagate chirally along the edge [40]. In contrast, at $\theta_\mathrm{H} = 0$, edge plasmons are absent, and since the boundary potential remains coupled to the bulk, the device response is determined by the bulk potential.

We find an exact analytic solution for this set of equations for arbitrary driving $\bar{V}(\varphi)$ by first considering that the solution of the Laplace equation, non-diverging at $r=0$, is an analytic function of the form

$$V(r,\varphi) = \sum_m v_m e^{im\varphi} \left(\frac{r}{R}\right)^{|m|} . \tag{10}$$

The coefficients v_m are determined by the boundary condition in equation (7) and are given by

$$v_m = \frac{\omega \bar{v}_m}{\omega - m\omega_R e^{i(\theta_H - \pi/2)m/|m|}} . \tag{11}$$

We now turn to a concrete example in which the boundary potential is defined by N electrodes. Each electrode j has angular length L_j^φ and extends from φ_j to $\varphi_{j+1} = \varphi_j + L_j^\varphi$, with $\varphi_1 = 0$ and $\varphi_{N+1} = 2\pi$. The applied boundary potential can then be written as

$$\bar{V}(\varphi) = \sum_{j=1}^{N} \left[\Theta\left(\varphi - \varphi_j\right) - \Theta\left(\varphi - \varphi_{j+1}\right)\right] \bar{V}_j , \tag{12}$$

where $\bar{V}_j$ is the potential applied to electrode j relative to a common ground. This potential has Fourier coefficients

$$\bar{v}_m = -i \sum_{j=1}^{N} \frac{e^{-im\varphi_j} - e^{-im\varphi_{j+1}}}{2\pi m} \bar{V}_j . \tag{13}$$

The potential V is then found by combining equations (10), (11), and (13). We note that the summation over Fourier harmonics can be performed exactly.

Here, we assumed the entire perimeter is covered by electrodes and neglect plasmon delays in ungated regions. This approximation is justified in the local capacitance approximation, where interactions in ungated segments are unscreened and plasmon velocities formally diverge [57]. More physically, the plasmon delay can be mimicked by smoothing the capacitance profile [40] instead of using step functions or by introducing fictitious grounded electrodes in ungated regions [49].

3.2. Microwave response

To evaluate the device response, we calculate the current I_i collected at electrode i when a potential $\bar{V}_j$ is applied to electrode j while all other electrodes are grounded. The current is obtained by integrating the time-dependent boundary charge density $i\omega\rho$ along the angular extent of electrode i. This procedure yields the terminal admittance matrix element

$$Y_{ij} = \frac{I_i}{\bar{V}_j} = i\omega\sigma_0 \sum_{m\neq 0} \frac{e^{i\left(\theta_H - \frac{\pi}{2}\right)\mathrm{sign}(m)} \left(e^{im\varphi_i} - e^{im\varphi_{i+1}}\right)\left(e^{-im\varphi_j} - e^{-im\varphi_{j+1}}\right)}{2\pi m \left(\omega - m\omega_R e^{i(\theta_H - \pi/2)\mathrm{sign}(m)}\right)} \tag{14a}$$

$$= \sigma_0 \left[F\left(\frac{\omega}{\omega_R}, \delta\varphi_{ij}, \theta_H\right) + F\left(\frac{\omega}{\omega_R}, \delta\varphi_{ij} + L_i^\varphi - L_j^\varphi, \theta_H\right) - F\left(\frac{\omega}{\omega_R}, \delta\varphi_{ij} + L_i^\varphi, \theta_H\right) - F\left(\frac{\omega}{\omega_R}, \delta\varphi_{ij} - L_j^\varphi, \theta_H\right)\right] , \tag{14b}$$

$$F(\omega,\varphi,\theta) = \frac{e^{i\varphi}\Phi\left(e^{i\varphi}, 1, 1 - \omega e^{-i(\theta-\pi/2)}\right) + \log\left(1 - e^{i\varphi}\right)}{i2\pi\, e^{-i(\theta-\pi/2)}} - \frac{e^{-i\varphi}\Phi\left(e^{-i\varphi}, 1, 1 + \omega e^{i(\theta-\pi/2)}\right) + \log\left(1 - e^{-i\varphi}\right)}{i2\pi\, e^{i(\theta-\pi/2)}} , \tag{14c}$$

where we introduced the angular distance $\delta\varphi_{ij} = \varphi_i - \varphi_j$ and $\Phi(a,b,c)$ is the Hurwitz-Lerch trascendent function.

We will now discuss various limits of this general result.

3.2.1. No Hall effect

When $\theta_H = 0$, the Hall effect is absent. In this case the material preserves time-reversal symmetry, and the response is fully reciprocal, such that the terminal admittance matrix satisfies $Y_{ij} = Y_{ji}$.

Although equation (14) can be evaluated directly at $\theta_H = 0$, further insight can be gained by expanding the response at small frequencies $\omega < |\omega_R|$. In this regime, the function F takes the form

$$F(\omega,\varphi,0) = -\sum_{k=1}^{\infty} (i\omega)^k \frac{\mathrm{Re}\left[\mathrm{Li}_{1+k}\left(e^{i\varphi}\right)\right]}{\pi} , \tag{15}$$

where $\mathrm{Li}_k(x)$ is the polylogarithmic function.

This expression shows that $F(0,\varphi,0)=0$, i.e. the system does not transmit DC signals. This behavior is consistent with the capacitive coupling at the boundary, which inherently blocks static responses and effectively decouples all terminals at $\omega=0$. At finite but small ω, the system response acquires both real and imaginary parts, corresponding respectively to dissipative and reactive contributions. Importantly, in this regime the response is non-universal and its precise value depends on the detailed geometry and edge profile of the Hall material [40].

3.2.2. Quantum Hall limit

An important regime of the terminal admittance matrix corresponds to the large magnetic field and low dissipation limit, defined by $\omega \ll \omega_c$ and $\omega_c\tau \to \infty$. This regime mimics the quantum Hall effect, where $\theta_{\mathrm{H}} \to \pi/2$, the diagonal elements of the conductivity tensor vanish, and the off-diagonal component reduces to $\sigma_0 = e^2\nu/h$, with filling factor $\nu = hn_S/eB$ [58]. We restrict ourselves to a positive magnetic field. In this limit, the plasmonic characteristic frequency becomes purely real-valued, yeilding $\omega_R = e^2\nu/hcR$. For typical values of capacitance $cR \approx 0.1$ pF [41] in GaAs, the characteristic frequency is in the microwave regime $\omega_R \approx \nu \times 0.4$ GHz and increases at lower magnetic field values.

The exact solution for the terminal admittance matrix takes the form [49, 51]

$$Y_{ij} = -\frac{\sigma_0}{2}\left[1 + i\cot\left(\frac{\pi\omega}{\omega_R}\right)\right]\left(1 - \mathrm{e}^{\frac{\mathrm{i}\omega L_i^{\varphi}}{\omega_R}}\right) \tag{16a}$$

$$\times \begin{cases} \left(1 - \mathrm{e}^{\frac{\mathrm{i}\omega\left(2\pi - L_i^{\varphi}\right)}{\omega_R}}\right) & i = j \\ \left(1 - \mathrm{e}^{\frac{\mathrm{i}\omega L_j^{\varphi}}{\omega_R}}\right)\mathrm{e}^{\frac{-i\omega\delta\varphi_{ji}^{\circlearrowleft}}{\omega_R}} & i \neq j \end{cases}, \tag{16b}$$

where $\delta\varphi_{ji}^{\circlearrowleft}$ denotes the angular separation between the right edge of electrode j (φ_{j+1}) and the left edge of electrode i (φ_i), measured in the clockwise direction.

Since at $\theta_{\mathrm{H}} = \pi/2$ the boundary dynamics are completely decoupled from the bulk potential (see equation (7)), this solution is universal and independent of the precise geometry of the quantum Hall material [40].

3.2.3. Circuit model for small dissipation

The lossless quantum Hall admittance matrix Y_{ij} in equation (16*a*) admits a simple interpretation in terms of an effective circuit model, see figure 1(b) [49, 51]. The device behaves as an ideal anticlockwise circulator with characteristic impedance

$$Z_c = \frac{1}{2\sigma_0}, \tag{17}$$

and scattering matrix

$$S_{\circlearrowleft} = \begin{pmatrix} 0 & 1 & 0 \\ 0 & 0 & 1 \\ 1 & 0 & 0 \end{pmatrix}, \tag{18}$$

which encodes the chirality of plasmon propagation, connected to each external terminal j via a stub impedance

$$Z_j(\omega) = \frac{i}{2\sigma_0}\cot\left(\frac{\omega L_j^{\varphi}}{2\omega_R}\right), \tag{19}$$

that accounts for the phase delay of plasmons due to their finite propagation velocity.

This circuit model provides an intuitive interpretation of the resonances observed in Hall effect devices. Beyond sharp edges, it also remains accurate for smoother boundary profiles emerging in electrostatically-defined edges [63, 64]. Moreover, it can be systematically generalized to capture slower plasmonic modes [57, 61] by introducing additional equivalent circuits connected in parallel, with appropriately rescaled values of σ_0 and ω_R in both Z_c and $Z_j(\omega)$ [51, 57].

We also emphasize that the proposed circuit model can be readily extended to include the finite plasmon delay time between electrodes that occur in real devices where metal gates are not covering the full perimeter. This extension can be implemented by introducing additional delay stubs with appropriately

chosen effective lengths (shorter than the physical distance between the edges of the electrodes) which capture the faster plasmon propagation along the unscreened edges [49, 51].

For small deviations of $\theta_{\rm H}$ from the ideal quantum Hall limit $\pi/2$, the equivalent circuit can be extended to account for dissipation by introducing complex-valued parameters,

$$\sigma_0 \to \sigma_0 \mathrm{e}^{\mathrm{i}(\theta_{\rm H}-\pi/2)\mathrm{sign}(\omega)} \quad \text{and} \quad \omega_R \to \omega_R \mathrm{e}^{-\mathrm{i}(\theta_{\rm H}-\pi/2)\mathrm{sign}(\omega)} \ . \tag{20}$$

This modification incorporates losses both in the plasmon propagation, through the dissipative stubs,

$$Z_j(\omega) = \frac{i\mathrm{e}^{-\mathrm{i}\left(\theta_{\rm H}-\frac{\pi}{2}\right)\mathrm{sign}(\omega)}}{2\sigma_0} \cot\left(\frac{\omega L_j^{\varphi}}{2\omega_R}\mathrm{e}^{\mathrm{i}\left(\theta_{\rm H}-\frac{\pi}{2}\right)\mathrm{sign}(\omega)}\right) \ , \tag{21}$$

and in the circulation itself, via the complex-valued impedance

$$Z_c = \frac{1}{2\sigma_0}\mathrm{e}^{-\mathrm{i}\left(\theta_{\rm H}-\frac{\pi}{2}\right)\mathrm{sign}(\omega)} \ . \tag{22}$$

Finally, we remark that the capacitance per unit length is $c \propto \epsilon_S$, where ϵ_S is the dielectric constant. Additional dielectric losses in the system can be incorporated within the our theoretical framework by introducing a complex-valued permittivity $\epsilon_S \to \epsilon_S' - i\epsilon_S''$, rendering the characteristic frequency ω_R complex-valued, in analogy to the effect of a finite longitudinal conductivity when $\theta_{\rm H} \neq \pi/2$.

4. Microwave devices

We now turn to concrete devices that serve as illustrative examples of equation (14).

4.1. Reciprocal two-terminal devices

To interpret the terminal admittance matrix in equation (14), we begin with the simplest geometry, that is a two-terminal device in which only two electrodes are coupled to the Hall material. This configuration is fully reciprocal, which can be intuitively understood from the circuit model of figure 1(b): with only two stubs present, no chirality-induced asymmetry arises.

The terminal admittance matrix in this case takes the general form

$$Y = Y_2 \begin{pmatrix} 1 & -1 \\ -1 & 1 \end{pmatrix} \ . \tag{23}$$

For symmetric electrodes of equal length $L_1^{\varphi} = L_2^{\varphi} = \pi$, the explicit expression becomes

$$\frac{Y_2}{\sigma_0} = \frac{\Phi\left(-1,1,1+\frac{\omega \mathrm{e}^{\mathrm{i}\left(\theta_{\rm H}-\frac{\pi}{2}\right)}}{\omega_R}\right) - \log(2) - H_{\frac{\omega \mathrm{e}^{\mathrm{i}\left(\theta_{\rm H}-\frac{\pi}{2}\right)}}{\omega_R}}}{i\pi\,\mathrm{e}^{\mathrm{i}\left(\theta_{\rm H}-\frac{\pi}{2}\right)}} - \frac{\Phi\left(-1,1,1-\frac{\omega \mathrm{e}^{-\mathrm{i}\left(\theta_{\rm H}-\frac{\pi}{2}\right)}}{\omega_R}\right) - \log(2) - H_{-\frac{\omega \mathrm{e}^{-\mathrm{i}\left(\theta_{\rm H}-\frac{\pi}{2}\right)}}{\omega_R}}}{i\pi\,\mathrm{e}^{-\mathrm{i}\left(\theta_{\rm H}-\frac{\pi}{2}\right)}} \ , \tag{24}$$

where H_x is the xth harmonic number.

We now restrict to real-valued ω_R and σ_0. Figure 2(a) shows the real (dashed curves) and imaginary (solid curves) parts of Y_2 as functions of frequency, for different values of the Hall angle $\theta_{\rm H}$. In the quantum Hall limit ($\theta_{\rm H} = \pi/2$, black curves), the expression simplifies to [40]

$$Y_2(\theta_{\rm H} = \pi/2) = -i\tan\left(\frac{\pi\omega}{2\omega_R}\right) \ . \tag{25}$$

The response is then purely imaginary, with resonances at $\omega = \omega_R(2n+1)$ and zeros at $\omega = \omega_R(2n)$. This behavior can be directly interpreted from the circuit of figure 1(b): the two-terminal admittance $Y_2 = 1/Z_1 + 1/Z_2$ reduces to the series combination of identical stubs $Z_1 = Z_2$ (equation (19)), which act as short circuits at resonance and open circuits at the zeros.

When small dissipation is included (blue curves), the sharp resonances broaden and their amplitude decreases with increasing frequency. When the Hall angle approaches zero (red curves), these resonant features vanish altogether, reflecting the absence of chiral plasmon propagation along the boundary in this limit.

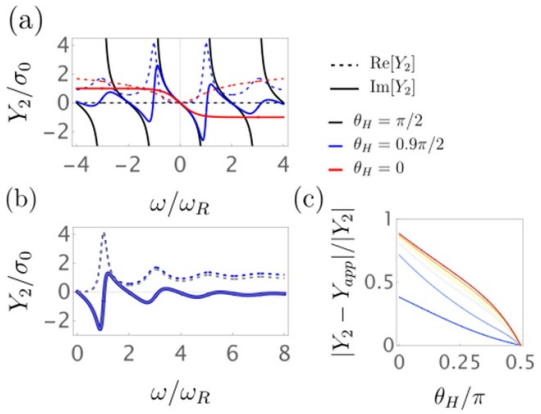

Figure 2. Reciprocal dissipative response. (a) Frequency dependence of Y_2 for varying Hall angle. We show real and imaginary components with dashed and solid lines. In the quantum Hall regime $\theta_{\rm H} = \pi/2$ (black curves) the system has resonances at $\omega = \omega_R$. These resonances are smoothed by dissipation, when the Hall angle decreases (blue curves), and are completely removed when $\theta_{\rm H} = 0$ (no Hall effect). (b) For small dissipation ($\theta_{\rm H} = 0.9\pi/2$) and low frequency, the response is accurately captured by our generalized dissipative circuit model (black solid and gray dashed line). (c) The error of this approximation is shown as a function of $\theta_{\rm H}$ for varying frequency, ranging from $\omega = 0.5\omega_R$ (blue curve) to $\omega = 5.5\omega_R$ (red curve) and varied with steps of ω_R.

In figure 2(b), we compare the exact analytic expression with the approximate dissipative circuit model of figure 1(b), using the substitutions in equation (20). For weak dissipation and low frequencies, the lossy stub model reproduces the smoothened resonances with high accuracy, and deviations appear only at higher-order resonances.

Moreover, in figure 2(c) we quantify the error as a function of $\theta_{\rm H}$ for different frequencies. The results confirm that the lossy stub circuit provides a quantitatively reliable description over a wide range of frequencies, provided dissipation and Hall angle remains small.

Finally, from the two-port admittance in equation (23), we can find corresponding scattering matrix through the textbook relation [65]

$$S = (I + Z_0 Y)^{-1} (I - Z_0 Y) \ , \tag{26}$$

where Z_0 is the characteristic real-valued impedance of the external circuit. Explicitly, defining the dimensionless complex-valued quantity $y = Z_0 Y_2$, we obtain

$$S = \frac{1}{1+2y} \begin{pmatrix} 1 & 2y \\ 2y & 1 \end{pmatrix} . \tag{27}$$

In lossy systems, the scattering matrix is generally not a unitary matrix and the variation from unitarity are physically related to the power dissipated. In this case, we find

$$I - S^\dagger S = \frac{\mathrm{Re}\,(y)}{|y|^2 + \mathrm{Re}\,(y) + 1/4} \begin{pmatrix} 1 & -1 \\ -1 & 1 \end{pmatrix} , \tag{28}$$

confirming that, as expected, the S-matrix is unitary, i.e. the system is lossless, at $\theta_{\rm H} = \pi/2$ since y is purely imaginary (see equation (25)), while dissipation caused by the real part of Y_2 is finite at $\theta_{\rm H} \neq \pi/2$, see figure 2.

4.2. Non-reciprocal three-port devices

We now turn to the response of non-reciprocal devices, focusing on the three-terminal geometry sketched in figure 1. For concreteness, we restrict here to symmetric electrodes of equal angular length $L_1^\varphi = L_2^\varphi = L_3^\varphi = 2\pi/3$, and evaluate equation (14) for this configuration. Although we emphasize the symmetric three-terminal case, our framework equally applies to multi-terminal devices with $N > 3$ as well as asymmetric electrode arrangements, such as the self-matched gyrator proposed in [50] and more recently realized in [44].

4.2.1. Symmetric gyrator

We first consider the gyrator [66]. An ideal gyrator is a two-port device characterized by the scattering matrix

$$S_G = e^{i\phi} \begin{pmatrix} 0 & -1 \\ 1 & 0 \end{pmatrix} . \tag{29}$$

where ϕ is an arbitrary phase.

Such a device can be implemented from our three-terminal Hall device simply by grounding one of the electrodes, e.g. electrode 3 [50]. Starting from the general terminal admittance matrix Y_{ij} in equation (14), which relates applied potentials to the resulting currents at all electrodes, we obtain a two-port admittance matrix by restricting Y_{ij} to the active electrodes $i,j \in 1,2$ while taking electrode 3 as grounded.

From this two-port admittance, the corresponding scattering matrix is obtained by using equation (26). In what follows, we assume that the Hall device is impedance-matched, i.e. $Z_0 = 1/(2\sigma_0)$. In the quantum Hall regime this condition is difficult to satisfy due to the large value of the resistance quantum ($1/\sigma_0 \approx 1/\nu \times 1/25\,\mathrm{k\Omega}$), but this requirement can be relaxed by operating at lower magnetic fields with large filling factors ν (a regime that is well-described by our model) or by appropriate geometrical modifications enabling self-matching [44, 50]. We delay an in-depth discussion on impedance matching to section 4.2.2.

From the scattering matrix, we define the standard non-reciprocity parameters

$$\Delta_\pm = \frac{S_{12} \pm S_{21}}{2} \quad \text{and} \quad \Delta_0 = \frac{S_{11} + S_{22}}{2} . \tag{30}$$

Here, the gyration parameter Δ_- quantifies the degree of non-reciprocity, being nonzero only in non-reciprocal devices [50]. In contrast, Δ_+ vanishes either for an ideal non-reciprocal device or when the device is fully reflective, i.e. when the relaxation parameter $|\Delta_0| = 1$.

Figure 3(a) shows the frequency dependence of these parameters in the symmetric gyrator. We compare the dissipationless limit (dashed lines) to the case of finite dissipation (solid lines). At low frequency, the device is always purely reflective. This behavior also recurs at $\omega = 3n\omega_R$. In contrast, at $\omega = (3n + 1/2)\omega_R$ the device behaves as an ideal gyrator, with perfect non-reciprocity.

This behavior admits a simple circuit interpretation, see figure 1(b). At $\omega = 3n\omega_R$, all three stubs $Z_1 = Z_2 = Z_3$ behave as open circuits, so the device is reflective. At $\omega = 3(n + 1/2)\omega_R$, the stubs instead act as short circuits, yielding an ideal non-reciprocal device.

For finite Hall angle (solid curves), the overall resonance pattern is unchanged, but part of the signal is lost and the amplitude of both transmitted and reflected components is reduced. The lowest-frequency resonances are less affected by dissipation, while higher-frequency ones are strongly suppressed. Finally, as shown in figure 3(a), the lossy circuit model obtained using equation (20), reproduces this behavior accurately (see dotted curves), capturing both the resonance structure and the dissipative smoothing.

4.2.2. Self-matched gyrator

High-impedance devices in quantum technologies can be advantageous in enabling the compact integration of part of the microwave circuitry directly on-chip, as well as potentially facilitating quantum coherent interfaces with small semiconducting systems such as quantum dots [29, 31]. However, when these devices are connected to standard external circuits where typically $Z_0 \sim 100\ \Omega$, the impedance matching condition $Z_0 = 1/(2\sigma_0)$ can be challenging to meet. In these cases, impedance matching techniques are required [65], for example by utilizing LC-circuits [41] and magnetic-field-resilient varactors [67].

An alternative approach is to design quantum Hall effect devices with a self-matched behavior [44, 50]. These devices not only do not require external impedance matching, but can intrinsically acts as on-chip impedance matchers for other high-impedance devices. The simple design for a self-match gyrator, requires the grounded electrode to be twice as long as the others, i.e. $L_3^\varphi = 2L_1^\varphi = 2L_2^\varphi$ [44, 50].

Figure 3(b) shows the parameters $\Delta_\pm$ in equation (30) as functions of frequency for the self-matched device. For concreteness, we consider here an impedance mismatch of $2\sigma_0 Z_0 = 1/5$, which corresponds for example to a realistic GaAs device at magnetic field $B = 0.5\,\mathrm{T}$ and $n_S = 10^{11}\,\mathrm{cm}^{-2}$, such that $\nu = 8$, matched with an external circuit with characteristic impedance $Z_0 \approx 300$ comparable to the vacuum impedance; moreover in this device, considering $cR \approx 0.1\,\mathrm{pF}$ [41], we find $\omega_R \approx 3.2\,\mathrm{GHz}$. We note that as expected from [50, 51], at $\theta_\mathrm{H} = \pi/2$, there are two ideal gyrating and one reflective peaks at low frequency. Finite Hall angles introduce losses that decreases the amplitudes of these peaks, a feature that is nicely captured by our effective lossy circuit model.

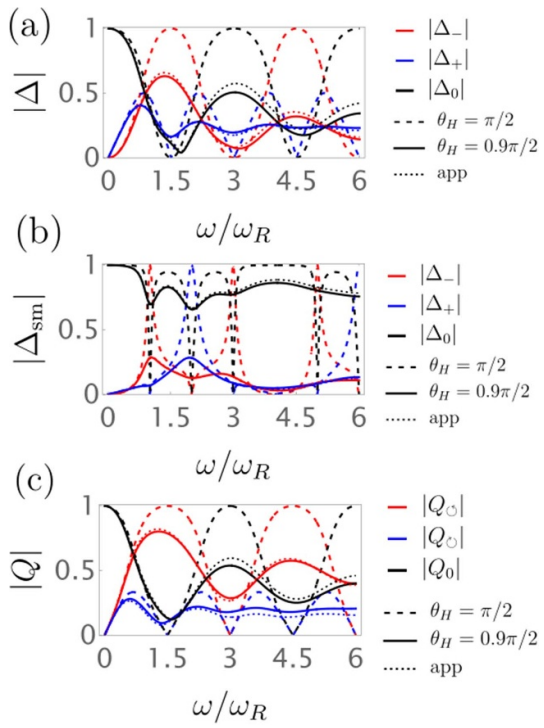

Figure 3. Non-reciprocal dissipative response. In (a), (c), we consider a device with three equal terminals impedance-matched with the external electrodes, i.e. $Z_0 = 1/2\sigma_0$. We operate the symmetric device as a two-port gyrator by grounding one electrode in (a) and as a three-port circulator in (c). In (b), we consider a self-matched gyrator with $Z_0 = 1/10\sigma_0$ with one grounded electrode twice as long as the others. We show relevant combinations of the scattering parameters as a function of ω. A finite Hall angle (solid curves) causes dissipation that decreases the amplitude of the transmitted signal as compared to the ideal quantum Hall device (dashed curves). The dampening of resonances is lower at low frequency where is well captured by our approximate dissipative circuit model (dotted curves).

4.2.3. Circulator

We now consider the three-port circulator [40, 41, 46], which is directly realized in the three-terminal Hall device by measuring the potential at each terminal with respect to a common ground. From the full three-dimensional terminal admittance matrix, the corresponding scattering matrix can be obtained using equation (26). As before, we focus on a matched device with $Z_0 = 1/2\sigma_0$.

To quantify the circulator's performance, we define the following parameters:

$$Q_{\circlearrowleft} = \frac{S_{12} + S_{23} + S_{31}}{3}\,, \tag{31a}$$

$$Q_{\circlearrowright} = \frac{S_{21} + S_{32} + S_{13}}{3}\,, \tag{31b}$$

$$Q_0 = \frac{S_{11} + S_{22} + S_{33}}{3}\,. \tag{31c}$$

Here, $Q_{\circlearrowleft}$ ($Q_{\circlearrowright}$) equals one for an ideal counterclockwise (clockwise) circulator (see equation (18)), while Q_0 quantifies reflection, reaching unity only for a fully reflective device.

Figure 3(c) shows these parameters as functions of frequency. The behavior mirrors that of the gyrator: the device is fully reflective at $\omega = 3n\omega_R$, while ideal non-reciprocal circulation is achieved at $\omega = 3(n+1/2)\omega_R$. For finite Hall angles, the amplitude of the circulating signals decreases, reflecting the dissipative losses, but the overall resonance pattern remains unchanged. As with the gyrator, this dissipative behavior is well captured by our lossy circuit model.

4.3. AC response of material

Our general model, and in particular the terminal admittance matrix in equation (14), not only captures dissipation but also includes the intrinsic AC response of the material. This originates from the fact that the conductivity tensor generally has a reactive component, for example due to kinetic inductance, leading to complex-valued σ_0 and $\theta_{\rm H}$ (see equation (3)). In our non-reciprocal device this modifies $\omega_R \propto \sigma_0$, which itself becomes complex (see equation (8)).

In figure 4, we analyze how the intrinsic AC response modifies the operation of the three-port symmetric circulator. Specifically, we plot the Q parameters defined in equation (31) as functions of both

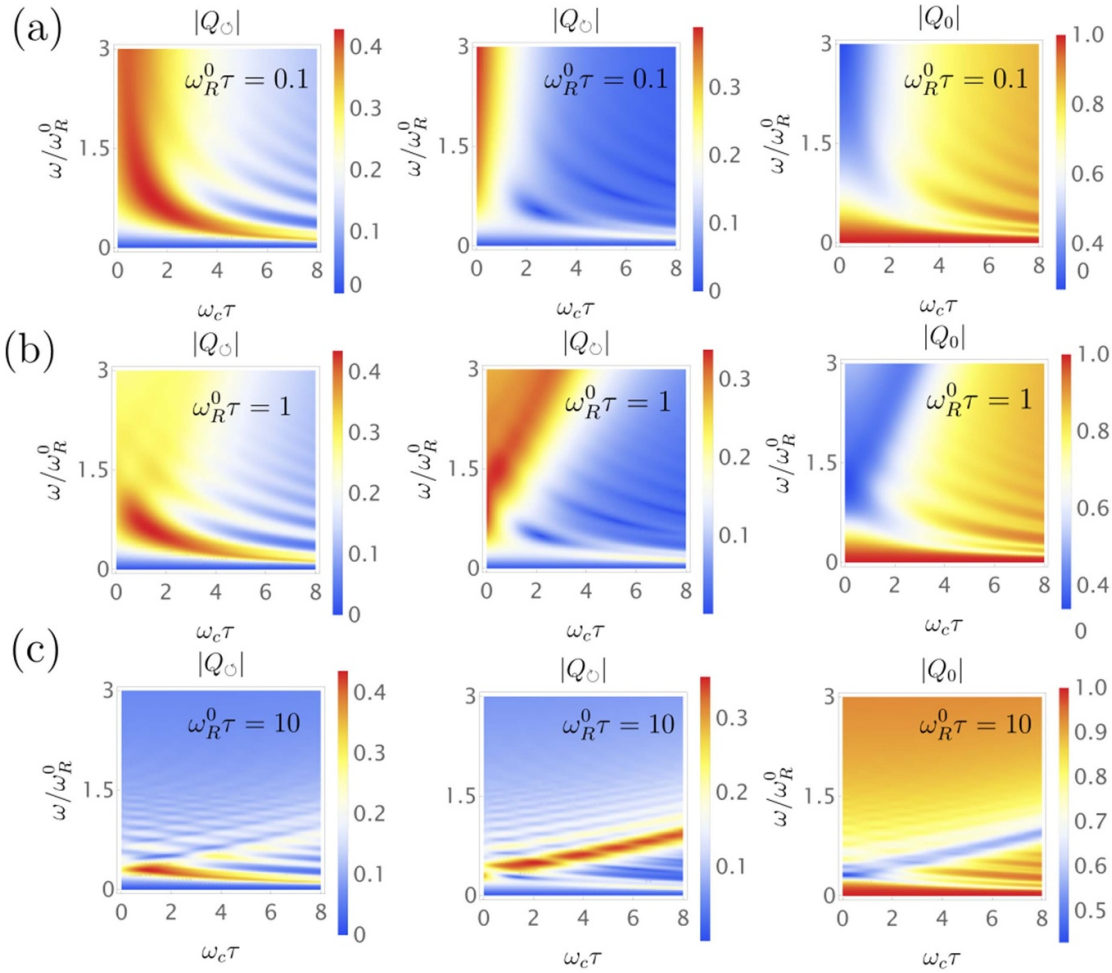

Figure 4. Intrinsic AC response. We consider the response of a three-port dissipative circulator, and show relevant combinations of scattering parameters against frequency (ω/ω_R^0) and magnetic field ($\omega_c\tau \propto B$). To capture the effect of an increasing magnetic field, the external electrodes are impedance-matched with the zero-frequency and zero-field characteristic impedance of the device, i.e. $Z_0 = 1/2\sigma_0(\omega = \omega_c = 0)$. In analogy, we normalize ω over $\omega_R^0 = \sigma_0(\omega = \omega_c = 0)/cR$, and the Hall angle is varied as $\theta_H = \arctan2(\omega_c\tau, 1 - \omega\tau)$. In rows (a), (b), and (c), we show the effect of an increasing value of the kinetic inductance of the device, parametrized by an increasing the product $\omega_R^0\tau$. Row (a) shows the response for negligible kinetic inductance, where we identify the typical $\propto 1/B$ resonance lines. As we increase the kinetic inductance, in row (b), additional counter rotating resonances $\propto B$ begin appear, that become sharp resonances at large kinetic inductance in row (c).

the frequency ω and the cyclotron frequency $\omega_c \propto B$, normalized by the scattering time τ. To capture the full dependence on the magnetic field B, we normalize frequencies by ω_R^0, defined as ω_R evaluated at $\sigma_0(\omega = \omega_c = 0)$. Similarly, we assume the external circuit to be matched to the real-valued resistance $Z_0 = 1/2\sigma_0(\omega = \omega_c = 0) = m^*/2e^2 n_S\tau$.

The intrinsic AC response of the material is encoded in the frequency dependence of $\sigma_0(\omega)$ and $\theta_H(\omega)$, both of which depend on the scattering time τ. At low frequencies, this dependence results in a kinetic inductance that renders the diagonal components of the conductivity tensor complex, i.e. $\sigma_{xx} \approx \sigma_{xx}(1 - i\omega\tau)$ [60]. To explore this effect, we vary τ normalized by ω_R^0.

In figure 4(a), we focus on the small kinetic inductance case. Here, we recover the expected $\omega_R \propto \sigma_0 \propto 1/B$ scaling of the resonance lines [41]. Here, we neglect the flattening of the resonances caused by quantum Hall plateaus. Dissipation suppresses higher-order resonances, leaving only the lowest ones visible. These results are consistent with previous numerical results for static dissipation in Hall devices [68].

At intermediate kinetic inductance, $\tau \sim \omega_R^0$ in figure 4(b), we observe a smoothening of the low-frequency, low-field counterclockwise resonance. At the same time, more resonant features begin to emerge in the clockwise circulation and in the reflection response.

At large kinetic inductance, in figure 4(c), these features evolve into sharp resonances with an opposite (clockwise) circulation compared to the expected chirality of the plasmons. Remarkably, these counter-circulating resonances scale $\propto B$, in contrast to the $1/B$ scaling of the direct plasmonic resonances.

We emphasize that while extrinsic circuit elements (such as parasitic capacitances) can also generate counter-circulating signals [41, 51], they typically retain the same $1/B$ scaling as the primary plasmonic resonances. The distinct B-scaling observed here clearly distinguishes these additional resonances arising from the intrinsic reactive response of the material.

Importantly, even in the lossy regime these counter-resonances remain as strong as the direct circulating features. This suggests a potentially practical route to selectively control the direction of signal propagation in Hall-effect based circulators.

5. Conclusion

In summary, we have developed a general analytic framework describing the microwave response of passive non-reciprocal devices, which naturally incorporates dissipation, geometric effects, and the intrinsic AC response of the underlying material. Our analytic solution provides clear physical interpretation of the system response in terms of a lossy stub circuit model, which we show accurately captures the device response in the experimentally relevant regime. Furthermore, by extending the model to include frequency-dependent conductivities, we revealed features, such as counter-circulating resonances with distinct magnetic field scaling, that are not captured by extrinsic circuit elements. Altogether, our results establish a unified description of microwave devices based on non-reciprocal materials, bridging microscopic material response and macroscopic circuit performance, and providing practical guidelines for designing next-generation compact non-reciprocal components.

Data availability statement

No new data were created or analysed in this study.

Acknowledgments

We thank David DiVincenzo for stimulating discussions. We are also grateful to Aldo Tarascio, Rafael Eggli, Miguel Carballido, Yiqi Zhao, and Dominik Zumbühl for constant insights and for sharing experimental data prior publication. This work was supported by NCCR Spin (Grant Number 225153).

ORCID iD

Stefano Bosco 0000-0002-4035-9654

References

[1] Barzanjeh S, Xuereb A, Alù A, Mann S A, Nefedkin N, Peano V and Rabl P 2025 Nonreciprocity in quantum technology (arXiv:2508.03945)
[2] Zou J, Bosco S, Thingstad E, Klinovaja J and Loss D 2024 Dissipative spin-wave diode and nonreciprocal magnonic amplifier *Phys. Rev. Lett.* **132** 036701
[3] Wang Y-Y, van Geldern S, Connolly T, Wang Y-X, Shilcusky A, McDonald A, Clerk A A and Wang C 2021 Low-loss ferrite circulator as a tunable chiral quantum system *Phys. Rev. Appl.* **16** 064066
[4] Fang K, Luo J, Metelmann A, Matheny M H, Marquardt F, Clerk A A and Painter O 2017 Generalized non-reciprocity in an optomechanical circuit via synthetic magnetism and reservoir engineering *Nat. Phys.* **13** 465
[5] Barzanjeh S, Wulf M, Peruzzo M, Kalaee M, Dieterle P B, Painter O and Fink J M 2017 Mechanical on-chip microwave circulator *Nat. Commun.* **8** 953
[6] Jiao Y-F, Zhang S-D, Zhang Y-L, Miranowicz A, Kuang L-M and Jing H 2020 Nonreciprocal optomechanical entanglement against backscattering losses *Phys. Rev. Lett.* **125** 143605
[7] Ahmadi B, Mazurek P, Horodecki P and Barzanjeh S 2024 Nonreciprocal quantum batteries *Phys. Rev. Lett.* **132** 210402
[8] Ando F, Miyasaka Y, Li T, Ishizuka J, Arakawa T, Shiota Y, Moriyama T, Yanase Y and Ono T 2020 Observation of superconducting diode effect *Nature* **584** 373
[9] Nadeem M, Fuhrer M S and Wang X 2023 The superconducting diode effect *Nat. Rev. Phys.* **5** 558
[10] Valentini M *et al* 2024 Parity-conserving cooper-pair transport and ideal superconducting diode in planar germanium *Nat. Commun.* **15** 169
[11] Ciaccia C, Haller R, Drachmann A C C, Lindemann T, Manfra M J, Schrade C and Schönenberger C 2023 Gate-tunable josephson diode in proximitized inas supercurrent interferometers *Phys. Rev. Res.* **5** 033131
[12] Trahms M *et al* 2023 Diode effect in josephson junctions with a single magnetic atom *Nature* **615** 628
[13] Daido A, Ikeda Y and Yanase Y 2022 Intrinsic superconducting diode effect *Phys. Rev. Lett.* **128** 037001
[14] Souto R S, Leijnse M and Schrade C 2022 Josephson diode effect in supercurrent interferometers *Phys. Rev. Lett.* **129** 267702
[15] Ilić S and Bergeret F S 2022 Theory of the supercurrent diode effect in rashba superconductors with arbitrary disorder *Phys. Rev. Lett.* **128** 177001

[16] Navarathna R, Le D T, Hamann A R, Nguyen H D, Stace T M and Fedorov A 2023 Passive superconducting circulator on a chip *Phys. Rev. Lett.* **130** 037001
[17] Le D T, Müller C, Navarathna R, Fedorov A and Stace T M 2021 Operating a passive on-chip superconducting circulator: device control and quasiparticle effects *Phys. Rev. Res.* **3** 043211
[18] Kumar N P, Le D T, Pakkiam P, Stace T M and Fedorov A 2025 Low-loss on-chip superconducting microwave circulator assisted by shunting capacitors *Phys. Rev. Res.* **7** 013075
[19] Riwar R-P, Houzet M, Meyer J S and Nazarov Y V 2016 Multi-terminal josephson junctions as topological matter *Nat. Commun.* **7** 11167
[20] Kashuba O, Mummadavarapu R and Riwar R-P 2024 Of gyrators and anyons (arXiv:2410.20835)
[21] Ingla-Aynés J, Hou Y, Wang S, Chu E-D, Mukhanov O A, Wei P and Moodera J S 2025 Efficient superconducting diodes and rectifiers for quantum circuitry *Nat. Electron.* **8** 411
[22] Castellani M, Medeiros O, Buzzi A, Foster R A, Colangelo M and Berggren K K 2025 A superconducting full-wave bridge rectifier *Nat. Electron.* **8** 417
[23] Rymarz M, Bosco S, Ciani A and DiVincenzo D P 2021 Hardware-encoding grid states in a nonreciprocal superconducting circuit *Phys. Rev. X* **11** 011032
[24] Rymarz M and DiVincenzo D P 2023 Consistent quantization of nearly singular superconducting circuits *Phys. Rev. X* **13** 021017
[25] Parra-Rodriguez A, Egusquiza I L, DiVincenzo D P and Solano E 2019 Canonical circuit quantization with linear nonreciprocal devices *Phys. Rev. B* **99** 014514
[26] Parra-Rodriguez A and Egusquiza I L 2025 Exact quantization of nonreciprocal quasilumped electrical networks *Phys. Rev. X* **15** 011072
[27] Javed M, Kruti D, Kenawy A, Herrig T, Koliofoti C, Kashuba O and Riwar R-P 2024 Utilizing and extending superconducting circuit toolbox to simulate analog quantum gravity (arXiv:2406.01261)
[28] Bartolomei H *et al* 2023 Observation of edge magnetoplasmon squeezing in a quantum hall conductor *Phys. Rev. Lett.* **130** 106201
[29] Bosco S and DiVincenzo D P 2019 Transmission lines and resonators based on quantum hall plasmonics: electromagnetic field, attenuation and coupling to qubits *Phys. Rev. B* **100** 035416
[30] Lin C, Futamata K, Akiho T, Muraki K and Fujisawa T 2024 Resonant plasmon-assisted tunneling in a double quantum dot coupled to a quantum hall plasmon resonator *Phys. Rev. Lett.* **133** 036301
[31] Elman S J, Bartlett S D and Doherty A C 2017 Long-range entanglement for spin qubits via quantum hall edge modes *Phys. Rev. B* **96** 115407
[32] Yang G, Hsu C-H, Stano P, Klinovaja J and Loss D 2016 Long-distance entanglement of spin qubits via quantum hall edge states *Phys. Rev. B* **93** 075301
[33] Arute F *et al* 2019 Quantum supremacy using a programmable superconducting processor *Nature* **574** 505
[34] Fay C and Comstock R 1965 Operation of the ferrite junction circulator *IEEE Trans. Microw. Theory Tech.* **13** 15
[35] Metelmann A and Clerk A A 2015 Nonreciprocal photon transmission and amplification via reservoir engineering *Phys. Rev. X* **5** 021025
[36] Metelmann A and Türeci H E 2018 Nonreciprocal signal routing in an active quantum network *Phys. Rev. A* **97** 043833
[37] Rosenthal E I, Chapman B J, Higginbotham A P, Kerckhoff J and Lehnert K W 2017 Breaking Lorentz reciprocity with frequency conversion and delay *Phys. Rev. Lett.* **119** 147703
[38] Chapman B J, Rosenthal E I, Kerckhoff J, Moores B A, Vale L R, Mates J A B, Hilton G C, Lalumière K, Blais A and Lehnert K W 2017 Widely tunable on-chip microwave circulator for superconducting quantum circuits *Phys. Rev. X* **7** 041043
[39] Chapman B J, Rosenthal E I and Lehnert K W 2019 Design of an on-chip superconducting microwave circulator with octave bandwidth *Phys. Rev. Appl.* **11** 044048
[40] Viola G and DiVincenzo D P 2014 Hall effect gyrators and circulators *Phys. Rev. X* **4** 021019
[41] Mahoney A C, Colless J I, Pauka S J, Hornibrook J M, Watson J D, Gardner G C, Manfra M J, Doherty A C and Reilly D J 2017 On-chip microwave quantum hall circulator *Phys. Rev. X* **7** 011007
[42] Petković I, Williams F I B, Bennaceur K, Portier F, Roche P and Glattli D C 2013 Carrier drift velocity and edge magnetoplasmons in graphene *Phys. Rev. Lett.* **110** 016801
[43] Kumada N, Tanabe S, Hibino H, Kamata H, Hashisaka M, Muraki K and Fujisawa T 2013 Plasmon transport in graphene investigated by time-resolved electrical measurements *Nat. Commun.* **4** 1363
[44] Tarascio A *et al* 2025 Self-matched quantum hall gyrator in preparation
[45] Mahoney A C, Colless J I, Peeters L, Pauka S J, Fox E J, Kou X, Pan L, Wang K L, Goldhaber-Gordon D and Reilly D J 2017 Zero-field edge plasmons in a magnetic topological insulator *Nat. Commun.* **8** 1836
[46] Martinez L A, Du N, Materise N, Kelley S O, Wu X, Qiu G, Wang K L, Gianpaolo P, Low T and Qu D-X 2025 Circulators based on coupled quantum anomalous hall insulators and resonators (arXiv:2505.07770)
[47] Gourmelon A *et al* 2023 Velocity and confinement of edge plasmons in hgte-based two-dimensional topological insulators *Phys. Rev. B* **108** 035405
[48] Röper T, Thomas H, Rosenbach D, Uday A, Lippertz G, Denis A, Morfin P, Taskin A A, Ando Y and Bocquillon E 2024 Propagation, dissipation and breakdown in quantum anomalous hall edge states probed by microwave edge plasmons *Phys. Rev. B* **110** L161403
[49] Bosco S, DiVincenzo D and Reilly D 2019 Transmission lines and metamaterials based on quantum hall plasmonics *Phys. Rev. Appl.* **12** 014030
[50] Bosco S, Haupt F and DiVincenzo D P 2017 Self-impedance-matched hall-effect gyrators and circulators *Phys. Rev. Appl.* **7** 024030
[51] Bosco S 2019 Quantum hall plasmonics for quantum computation *PhD Thesis* (https://doi.org/10.18154/RWTH-2019-09498)
[52] Lodari M, Kong O, Rendell M, Tosato A, Sammak A, Veldhorst M, Hamilton A R and Scappucci G 2022 Lightly strained germanium quantum wells with hole mobility exceeding one million *Appl. Phys. Lett.* **120** 122104
[53] Goerbig M O 2011 Electronic properties of graphene in a strong magnetic field *Rev. Mod. Phys.* **83** 1193
[54] Bestwick A J, Fox E J, Kou X, Pan L, Wang K L and Goldhaber-Gordon D 2015 Precise quantization of the anomalous hall effect near zero magnetic field *Phys. Rev. Lett.* **114** 187201

[55] Novoselov K S, Jiang Z, Zhang Y, Morozov S V, Stormer H L, Zeitler U, Maan J C, Boebinger G S, Kim P and Geim A K 2007 Room-temperature quantum hall effect in graphene *Science* **315** 1379
[56] Fetter A L 1985 Edge magnetoplasmons in a bounded two-dimensional electron fluid *Phys. Rev. B* **32** 7676
[57] Bosco S and DiVincenzo D P 2017 Nonreciprocal quantum hall devices with driven edge magnetoplasmons in two-dimensional materials *Phys. Rev. B* **95** 195317
[58] Girvin S M 2002 The quantum hall effect: Novel excitations and broken symmetries *Aspects Topologiques de la Physique en Basse Dimension. Topological Aspects of low Dimensional Systems: Session Lxix. 7–31 July 1998* (Springer) pp 53–175
[59] Chang C-Z, Liu C-X and MacDonald A H 2023 Colloquium: quantum anomalous hall effect *Rev. Mod. Phys.* **95** 011002
[60] Volkov V and Mikhailov S A 1985 Theory of edge magnetoplasmons in a two-dimensional electron gas *JETP Lett.* **42** 556–60
[61] Aleiner I L and Glazman L I 1994 Novel edge excitations of two-dimensional electron liquid in a magnetic field *Phys. Rev. Lett.* **72** 2935
[62] Johnson M D and Vignale G 2003 Dynamics of dissipative quantum hall edges *Phys. Rev. B* **67** 205332
[63] Chklovskii D B, Shklovskii B I and Glazman L I 1992 Electrostatics of edge channels *Phys. Rev. B* **46** 4026
[64] Chamon C d C and Wen X G 1994 Sharp and smooth boundaries of quantum hall liquids *Phys. Rev. B* **49** 8227
[65] Pozar D M 2012 *Microwave Engineering* (*University of Massachusetts at Amherst*) 4th edn (Wiley)
[66] Tellegen B D 1948 The gyrator, a new electric network element *Philips Res. Rep.* **3** 81
[67] Eggli R S *et al* 2023 Cryogenic hyperabrupt strontium titanate varactors for sensitive reflectometry of quantum dots *Phys. Rev. Appl.* **20** 054056
[68] Placke B, Bosco S and DiVincenzo D P 2017 A model study of present-day hall-effect circulators *EPJ Quantum Technol.* **4** 5